

A novel approach to the realisation of a rail specimen with defined surface cracks in work-hardening manganese steel for the calibration of inductive thermographic measurements

by C. Tuschl*, B. Oswald-Tranta*, D. Künstner**, S. Eck***

* University of Leoben, Peter-Tunner Strasse 25, 8700 Leoben, Austria, christoph.tuschl@unileoben.ac.at

**voestalpine Rail Technology GmbH, Kerpelystraße 199, 8700 Leoben, Austria,
david.kuenstner@voestalpine.com

***Materials Center Leoben Forschung GmbH, Roseggerstraße 12, 8700 Leoben, Austria, sven.eck@mcl.at

Abstract

Induction thermography is a well-established method for the detection of surface defects in magnetic steel. Furthermore, static inductive measurements are used to estimate the depths and penetration angles of surface cracks. This work presents a new approach to creating crack-like, but defined surface defects in a manganese steel rail specimen. Cuts with different penetration depths and angles are introduced into the head of the rail via wire erosion. The work-hardening behaviour of manganese steel allows for the cuts being closed by subsequent roll-overs performed on a full-scale wheel-rail test rig. This improves the calibration of the parameters used for the specification of crack depth and penetration angle during measurements of rolling contact fatigue damage in track.

1. Introduction

Inductive thermography is a non-destructive testing method (NDT) that is often used to detect surface defects in metallic parts. During a static measurement the excitation of a specimen is performed with a short inductive heating pulse ($t \leq 1$ s), heating mainly the surface of the specimen ($\Delta T < 10$ K). This change in surface temperature is recorded via infrared camera. As eddy currents and the resulting heating are influenced by cracks and surface defects, these changes are visible in the recorded infrared sequence. Inductive thermography is a normed method, characterized in particular as a fast and contactless NDT-method which allows automation and is therefore suitable for in-line testing in production [1–3]. Furthermore, static method allows the estimation of a crack's depth and penetration angle. In Ref. [4] it is demonstrated that phase images—generated through a pixel-wise Fourier transform of the recorded image sequence—can be utilized to estimate these parameters. Phase values change in the vicinity of a crack, indicating the direction and depth of a crack under the surface. However, phase images are highly dependent on both material and excitation parameters, necessitating the use of simulations and calibration bodies for adequate estimation. With advancements in the spatial resolution of infrared (IR) cameras, there is an increased demand for such calibration bodies for accurate characterization. While manufactured cuts are often clearly visible to the IR camera even without excitation due to their width, producing thinner cuts remains an expensive process.

Manganese steel has become a standard for high-quality turnout frogs due to preferable mechanical properties. Its work hardening behaviour allows for initial deformation of the wheel rail contact area of turnout frogs, reducing the contact forces of rail and wheel. After this initial stage manganese steel shows high toughness and good wear resistance [5]. However, the coarse grain structure of this material affects NDT-methods such as ultrasonic and eddy current testing, two methods commonly used in the railway industry. This demands improvements on established methods, as well as the research into new methods for railway applications [6,7]. Researchers worldwide are looking into inductive thermography for railway application [8–11] and Ref. [7] shows, that this method also works for manganese steel turnout frogs.

This work presents a novel approach to create defined cracks in a calibration body made from a manganese steel rail piece. The main goal is to create a realistic reference for characterising surface cracks in manganese turnout frogs. Wire eroding (EDM) was used to introduce 80 defined cuts with specified depths and penetration angles at both gauge corners of a one-meter-long manganese rail piece. On a full-scale wheel-rail test rig one gauge corner is then rolled-over by a wheel to slightly deform the surface at the wheel rail contact region and therefore close the cuts on the surface. The closed cuts correlate better with simulations and real cracks, since unwanted readings are generated at the bottom of open cuts.

This work is structured as follows: At first, the manufacturing process of the specimen is described in detail, as this is the main contribution of this work. Afterwards, the test setup to perform the inductive measurements is described, followed by a description of the performed finite element simulations conducted in ANSYS. The subsequent section presents results and comparisons before and after the roll over process. Finally, the paper concludes with a summary as well as a discussion.

2. Manufacturing process of the calibration specimen

This section explains the geometry and position of the cuts on the rail head and how the manufacturing was performed. The geometry of the cracks was visually inspected, which is also documented in this part.

2.1. Definition of rail cuts

The cuts are strategically located on both gauge corners of the one-meter-long rail. Due to the curvature of the gauge corner, various penetration angles and depths can be achieved using wire erosion. This area is significant because common surface defects, such as Head Checks, typically emerge here.

The cross-section of the rail head (Figure 1.a) shows that the bottom of each cut is angled at 30° relative to a horizontal line. This is the entry angle of the EDM wire into the material. The wire then cuts each section according to the specified depth and penetration angle, one at a time. Figure 1.b illustrates the definition of these parameters, where the penetration angle is defined as the angle between a cut and a line on the gauge corner in the driving direction.

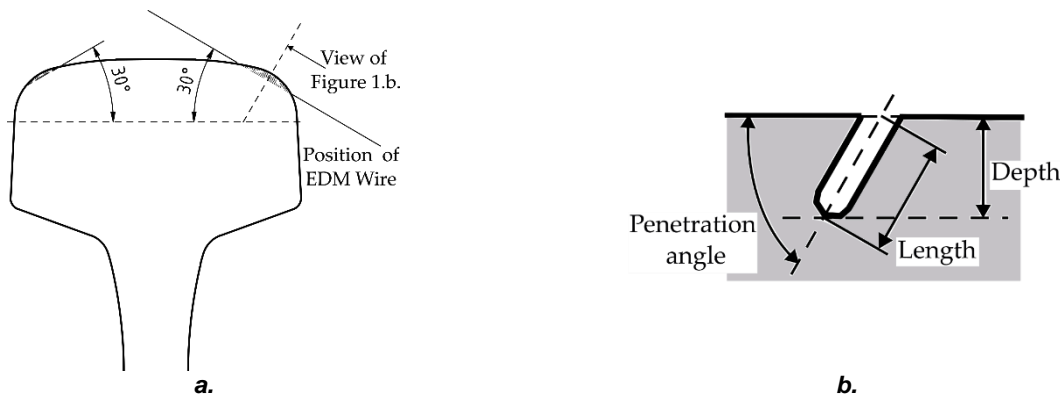


Figure 1. a. cross-section-sketch of the rail head showing the angle of penetration for the EDM wire; **b.** Definition of penetration angle, depth and length of a cut

The cuts were categorized into different sets and introduced into the rail piece as follows:

- First Set: This set consists of cuts that vary in depth from 2.0 mm to 0.5 mm in steps of 0.25 mm. They are perpendicular to the rail surface, illustrated in Figure 2.a.
- Second Set: These cuts have a penetration angle of 45° and vary in length from 2.0 mm to 0.5 mm in steps of 0.25 mm (Figure 2.b), which results in varying depths.
- Third Set: This set varies in penetration angle from a straight cut at 90° to 15° in steps of 15°, as shown in Figure 2.c. All cuts in this set have the same length of 1 mm.

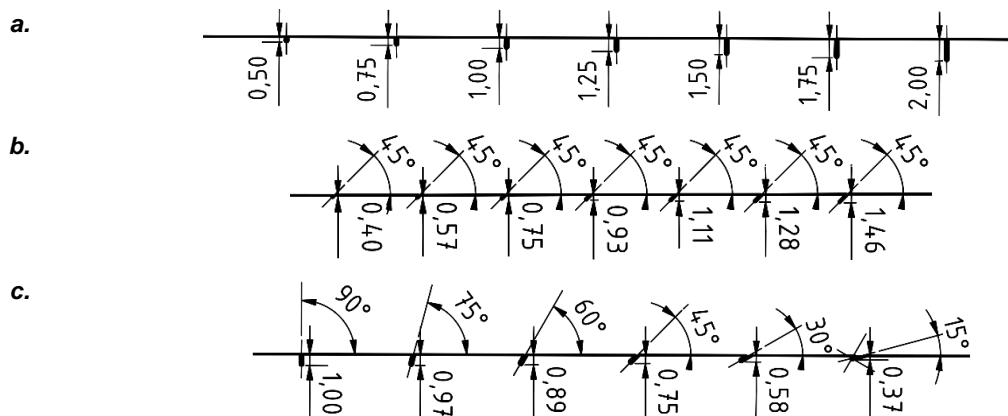


Figure 2. Sketches of the three different sets of cuts; a. perpendicular to the surface with cut depths from 2.0 mm to 0.5 mm; **b.** cuts with a penetration angle of 45° and cut lengths from 2.0 mm to 0.5 mm; **c.** cuts with penetration angles from 90° to 15° with cut length of 1 mm

Sets have been placed on both gauge corners of the rail. The goal is to further process the cuts on one side via rolling over and keep cuts on the other side as a reference. The 3 sets were introduced in duplicate on both sides resulting in a total of 12 sets or 80 cuts. In Figure 3 the location of all the sets on the rail piece is presented.

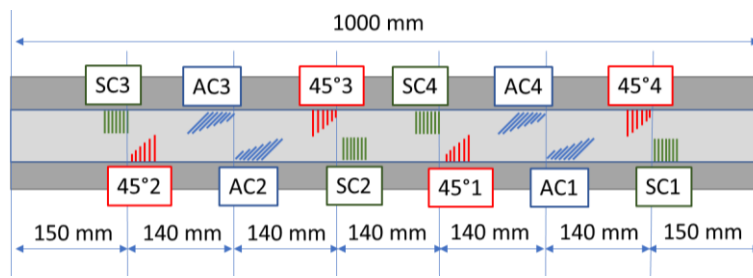


Figure 3. Sketch depicting the location of the 12 sets of cuts; SC stands for a set of straight cuts with varying depth, 45° for cuts with 45° penetration angle and varying depth and AC for angled cuts with the same length

2.2. Precision of wire EDM cutting

Figure 4.a shows the manganese steel rail and Figure 4.b a closer look on a set of straight cuts. All 80 cuts were made using an EDM-wire with a diameter of 0.25 mm which results in a cutting width of 0.35 mm (see Figure 4.c). Since measuring the exact depth of each cut is challenging, the surface length of each cut, which can be thought of as the arc length of the cut, was measured instead. These measured lengths were then compared to lengths from the CAD model (where the depths are easily measured) to evaluate the actual depths of each cut.

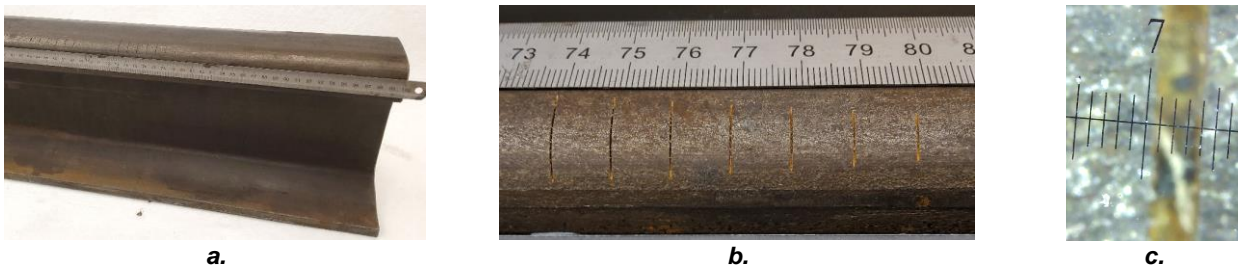


Figure 4. a. Picture of the manganese steel rail with EDM-cuts; b. Close-up look at the set of straight cuts; c. Measurement of the cutting width of a single straight cut

The evaluation of cut depths for sets one and two is shown in Figure 5. The cut depths and arc lengths from the CAD model were used to fit a third-degree polynomial. Arc lengths from both the CAD model and the different sets were plotted on the fitted line to visualize the estimated depth of each cut in the mid part. Cuts, which should have the same depth, are depicted with the same colour. For both straight cuts and cuts with a 45° penetration angle, the actual cuts on the specimen are deeper than those in the CAD model (see Figure 5.a. and c.). In the case of cuts with different penetration angles, the actual cut depths show no such trend and vary from the expected cut depths taken from the CAD-model (see Figure 5.b).

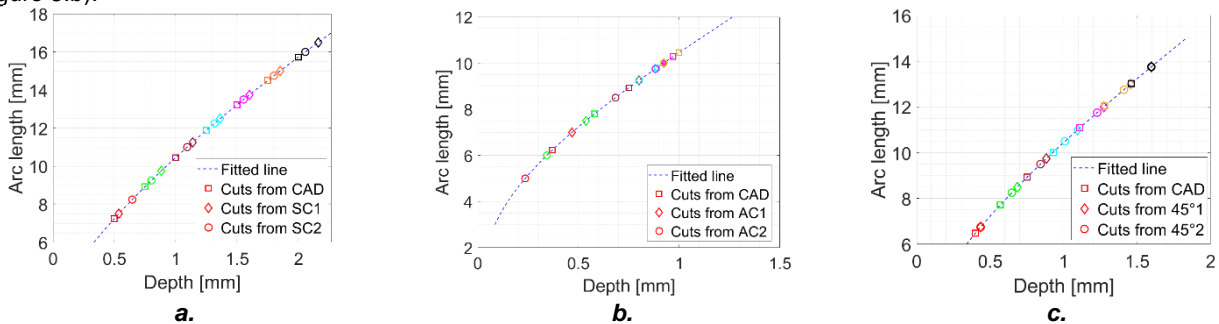


Figure 5. Arc length vs. depth plots for a. straight cuts; b. cuts with varying penetration angles; c. cuts with a 45° penetration angle

2.3. Closing cuts via rolling over

A full-scale wheel-rail test rig, operated at voestalpine Rail Technology GmbH, was used to close the cuts on one gauge corner containing the sets three and four. This test rig, shown in Figure 6.a, is normally used for high cycle fatigue tests of wheels and especially for rails. It is fully automated and parameters such as speed, roll-over cycles as well as the normal and lateral forces can be set and also adjusted during the test. The experiment to close the cuts on the gauge corner a normal force equivalent to 20 tons and a lateral force equivalent to 4 tons of mass was used. The speed was set to 0.5 m/s and the roll over only was performed in one direction. After one roll over the wheel was lifted from the rail and set back to the starting position (see Figure 6.b).



Figure 6. a. Image of the full-scale rail wheel test rig published in [12]; **b.** initial position of the wheel over the rail

In total 1000 roll-overs have been carried out, with multiple stops in between to document the progress with photos as well as microscopic images. Figure 7. highlights the progress of a single straight cut after 400, 600 and 1000 roll-overs. Microscopic images were taken at each stop and stitched together to show the entire cut. The result suggests, that contact between rail and wheel were best at the centre of the cut, as this area is completely closed. At the top and surface region a small opening still remains.

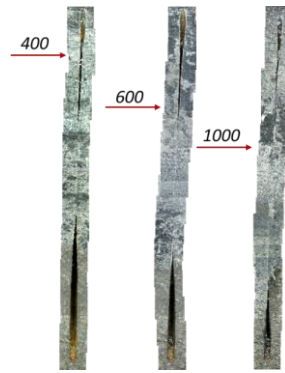


Figure 7. Progression of a straight cut closing during roll over. Each image consists of multiple micrographs.

The profile of the rail was measured via laser scanning before and after the roll-over experiment (see Figure 8.a). The upper part of the gauge corner was squeezed inwards due to the rolling over, whereas the lower area was squeezed outwards. This plastic deformation, which was achieved by the exaggerated loading conditions in the 1:1 wheel-rail test rig, is similar to the behaviour of explosion depth-hardened manganese steel turnout frogs during operation in track as reported by Oßberger et al [5]. The calculated difference of both profiles is illustrated in Figure 8.b. From CAD-data the location where the EDM-wire enters the material, thus the location where the cut is the deepest, is known. For the subsequent measurements, it is assumed that cut depths at this position are 0.1 mm shorter than before the plastic deformation.

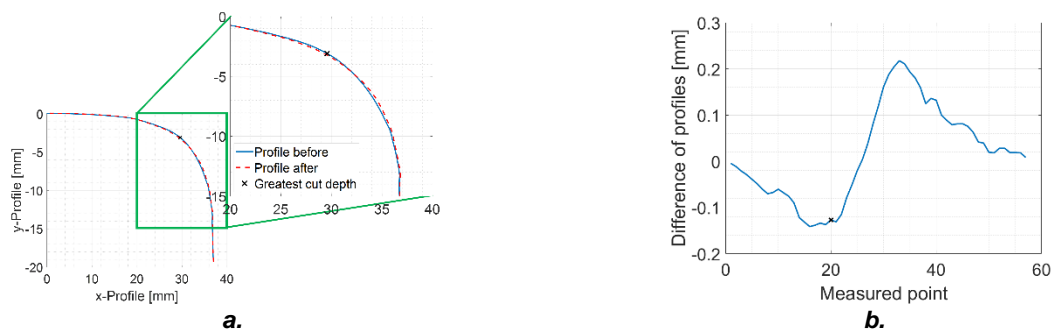


Figure 8. a. Profile of the gauge corner before and after the roll-over experiment; **b.** Difference along the profile due to roll-over; a black cross marks the greatest cut depth.

3. Measurement setup

For the static inductive measurements presented in this work a quantum-detector camera and an air-cooled inductor were used (see Figure 9.a). The camera (IRCam Velox 1310k SM [13]) records 1280 × 1024 pixels with a framerate of 180 Hz and has a noise equivalent temperature difference (NETD) of 0.25 mK. In this setup a 50 mm lens was used resulting in a resolution of 17.03 pixels per mm.

Generator (UNICUM VHF) and inductor (Cracky LT) are both commercial products of the company IFF GmbH. The excitation frequency of this air-cooled generator can be set between 25 and 60 kHz and induction pulses up to 500 ms are possible. For the measurements on the rail head an excitation frequency of 25 kHz and a pulse length of 300 ms was used. The inductor is also air-cooled and consists of a u-shaped ferritic core with copper wiring around it. It is especially shaped for inductive measurements as it allows an infrared camera to look directly at the heated area of a specimen in the centre (see Figure 9.b).



Figure 9. a. Laboratory setup for static inductive measurements on a rail head; b. Close-up of the inductor

4. Finite element simulations with ANSYS

For the interpretation of measurement results on open and closed cuts, finite element simulations were performed using ANSYS Multiphysics. The inductive excitation of cuts was modelled by coupling electromagnetic induction with a subsequent thermal calculation. A section of a rail gauge corner including a cut and a simplified inductor was used as the model (see Figure 10.a.). The depth, angle, and opening width of the cut were varied to perform a parameter study. The excitation frequency was set to 25 kHz, consistent with the measurements. The grid size of the rail gauge corners mesh is adapted according to the geometry of the cut as well as the excitation frequency to properly resolve the penetration depth of the eddy current. Figure 10.b illustrates, that the mesh grid on the surface becomes denser as it nears the cut. The pulse duration was set slightly shorter than in the measurements, at 250 ms. This adjustment accounts for the non-instantaneous nature of the real pulse, allowing for better comparability of the results between the simulation and actual measurements. A cooling-time of the same duration as the heating is also simulated. The material properties of manganese steel used in the simulation are summarized in Table 1. The surface temperatures calculated at each time step is recorded and saved for further evaluation (see Figure 10.c).

Table 1. Material properties of Mn13 used in the simulation

Electrical conductivity	$1.47 \cdot 10^6$ [1/Ω m]
Thermal conductivity	13 [W/m K]
Specific heat	500 [J/kg K]
Mass density	7900 [kg/m ³]

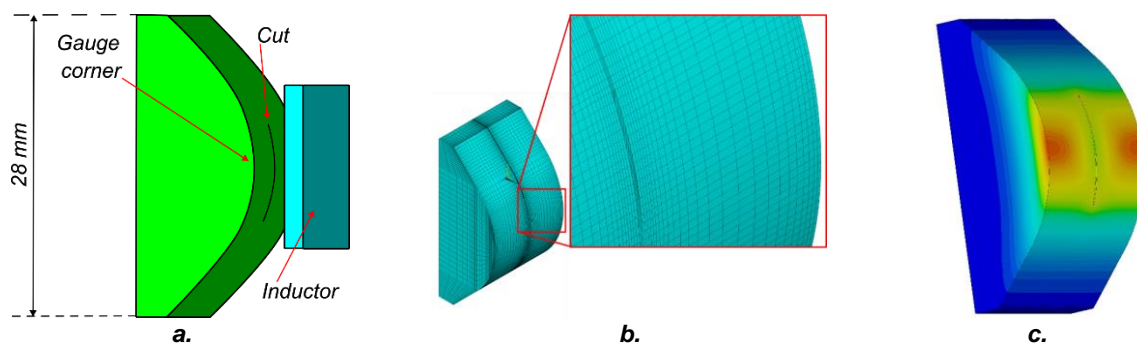


Figure 10. a. ANSYS model of the gauge corner of a rail and a simplified inductor; b. Mesh of the rail gauge corner model, c. Temperature distribution on the surface after a heating pulse.

The simulation data is loaded into MATLAB for further analysis, where a Fourier transform is applied to generate phase images, consistent with the evaluation method used for the inductive measurements. Prior to the Fourier transform, the simulation data points are meshed to a regular grid to ensure equidistant surface temperature data, addressing the dense mesh around the cut area. Both heating and cooling phase data are utilized in the Fourier transform process.

Figure 11.a shows the phase value changes due to the presence of the cut, with the cut area highlighted in red. Given the rail heads geometry and the cut inside of it, the depth of the cut is evaluated at the centre of a cut. This applies to the simulation as well as for the measurement results. Line profiles through this geometrical centre (shown in Figure 11.b) are used to assess and interpret the measurements, as well as the changes observed between open and closed cuts. On the y-axis the phase difference compared to the defect-free surface value is plotted.

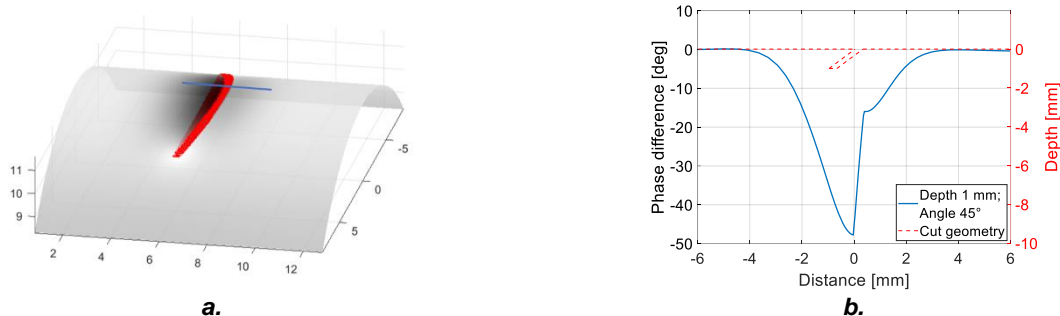


Figure 11.a. 3D illustration of phase values on the rail surface influenced by a cut of 1 mm depth and a penetration angle of 45°; **b.** Evaluation of the blue line profile shown in **Figure 11.a**

5. Results

All cuts, open on one gauge corner and closed on the other, have been measured using static inductive thermography. For some of the cuts ANSYS simulations have been performed using the calculated cut depth and the measured opening width of the cut. As shown previously, closing the cut via heavy plastic deformation reduces its depth by approximately 0.1 mm. Therefore, the simulations of closed cuts are performed with this reduced depth and narrower opening width. In this section the results of both are compared.

5.1. Comparison on straight cuts

For straight cuts, an open cut with a measured depth of 1.14 mm is presented. Thus, the simulation has been performed, using this measured depth and an opening width of 0.3 mm. The results are shown in Figure 12.a. to c. A comparison of the phase images from simulation (Figure 12.a.) and measurement (Figure 12.b.) shows, that the opening of the cut is clearly visible in the measurement. Notably, the phase values inside the cut differ significantly, likely due to contaminants that are heated differently during the measurement.

The line profile through the centre of both phase results demonstrates a good correlation between the simulation and the measurement (see Figure 12.c.), except for the irregularity caused by the open cut. This irregularity affects the minimum phase value, which is a key indicator used to estimate crack depths.

The closed cut was simulated using a depth of 1.04 mm and 0.15 mm opening width and the resulting phase image is presented in Figure 12.d. Due to the rolling over the phase image of the measurement (see Figure 12.e.) is noisier than before but the main goal, closing the cut, was achieved. The line profiles (see Figure 12.f.) indicate, that the cut is not as deep as estimated, since the minimum phase value of the measurement profile is less. The assumption that not only the cut depth but also the opening width needs to be reduced in the simulation aligns well with the data, as the new profiles are narrower than those for open cuts.

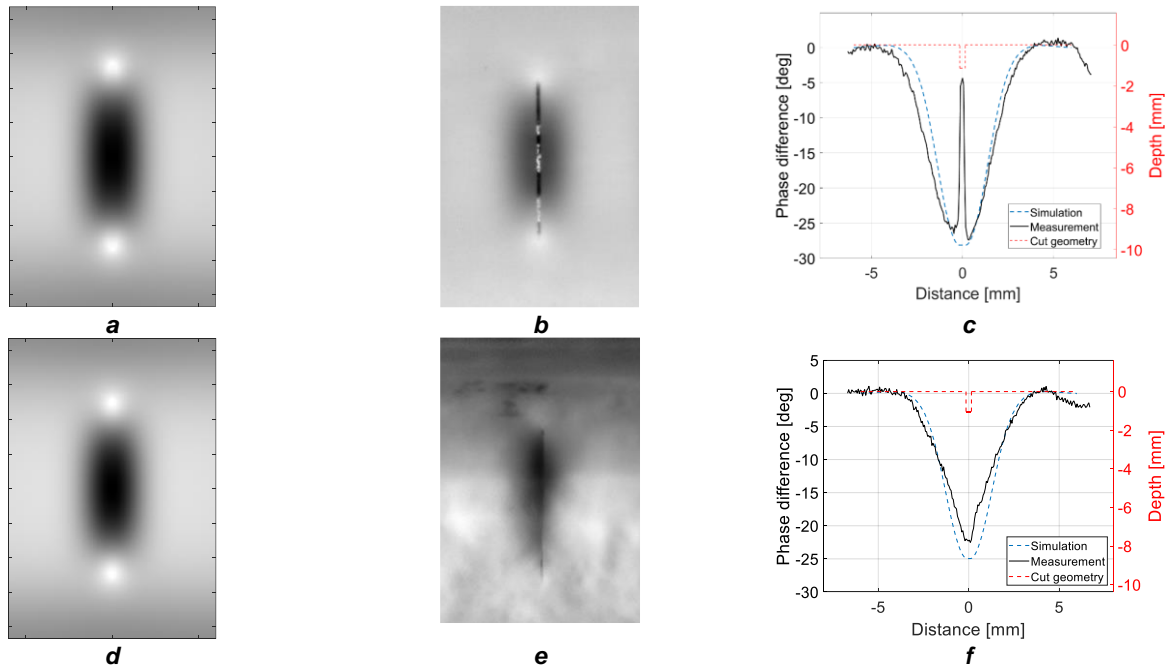


Figure 12. Results for straight cuts: **a.** Simulated phase image of the open cut; **b.** Phase image of the measured open cut; **c.** Comparison of line profile through the open cut; **d.** Simulated phase image of the closed cut; **e.** Phase image of the measured closed cut; **f.** Comparison of line profile through the closed cut

5.2. Comparison on cuts with 45° penetration angle

The same approach used for the straight cuts was applied for the evaluation of results on cuts with a 45-degree penetration angle. An open cut with a measured depth of 1.27 mm has been simulated with an opening width of 0.3 mm. Phase images of simulation (see Figure 13.a.) and measurement (see Figure 13.b.) are comparable; however, the cut is still visible in the measurement. The evaluation of the line profile reveals a significant difference in minimum values (see Figure 13.c.). While the simulation shows more than a 30-degree difference between the left and right sides of the cut, the measurement shows only a 12-degree difference.

For the simulation of the closed cut a depth of 1.17 mm and an opening width of 0.15 mm were used (see Figure 13.d.). The phase image from the measurement (see Figure 13.e.) shows that cut has been closed successfully. Both phase images are very similar. The line profile of the simulation in Figure 13.f indicates no significant change from open cut (compare with Figure 13.c.) to closed cut, despite the different depths and opening widths. The changes in the measured profile are more pronounced. The profile for the open cut in Figure 13.c. shows a pronounced asymmetry between left and right sides of the cut, whereas this asymmetry is less pronounced in Figure 13.f. The minimum phase value did not change significantly, even though the closed cut should be not as deep.

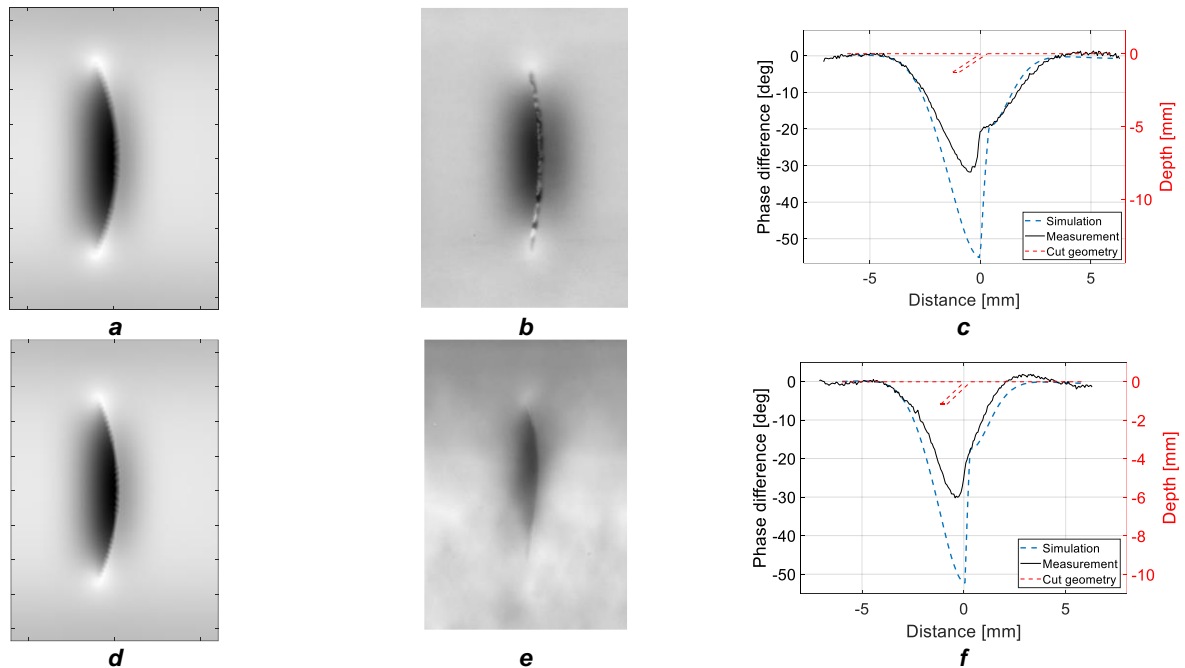


Figure 13. Results for cuts with 45° penetration angle: **a.** Simulated phase image of the open cut; **b.** Phase image of the measured open cut; **c.** Comparison of line profile through the open cut; **d.** Simulated phase image of the closed cut; **e.** Phase image of the measured closed cut; **f.** Comparison of line profile through the closed cut

6. Summary and conclusion

Eighty cuts were introduced to the gauge corners of a manganese steel (Mn13) rail. These cuts, with varying depths and penetration angles, serve as a calibration body for crack characterization using static inductive thermography. A novel aspect of this calibration body is that half of the cuts were closed on the surface using a full-scale rail-wheel test rig. This method gives the cuts a more realistic crack-like appearance, both in visual images and in the evaluation of thermographic image sequences. The goal is to enhance methods for characterizing surface cracks in manganese steel rail components. In this work the improvement of evaluation via phase images is investigated. The results show, that cuts were successfully closed with the new methodology, with slight openings at the end of the cuts.

For straight cuts, the comparison with simulations indicates an improvement due to the closing process. When evaluating a line profile through the centre of a cut, the open cuts exhibit anomalies in the centre. This is caused by the temperature data inside the cuts, which is also evaluated. Thus, these anomalies cannot appear while evaluating closed cuts. Additionally, to simulate the open cuts accurately, the opening width of the cuts must be adjusted accordingly. For the closed cuts, the opening widths can be significantly reduced, which correlates better with real cracks.

These benefits are also true for the evaluation of cuts with various penetration angles. However, there remains a significant difference in phase minima between simulation and measurement results for angled cuts. This discrepancy requires further investigation to understand the influences causing this difference between simulation and measurement of angled cuts. The manufacturing of calibration targets is time-consuming and cost intensive. However, once the accuracy of both the manufacturing and the simulations have been assessed, simulation-based data sets can be generated to serve as a basis for measuring rolling contact fatigue damage in track, e.g., through machine learning assisted evaluation.

7. Acknowledgements

The authors gratefully acknowledge the financial support by the IC-MPPE Company Project Partners ÖBB-Infrastruktur AG and voestalpine Railway Systems GmbH as part of the COMET IC-MPPE program.

The COMET “Integrated Computational Material, Process and Product Engineering (IC-MPPE)” Program (Project 886385) within the K2 Center is supported by the Austrian Federal Ministries for Climate Action, Environment, Energy, Mobility, Innovation and Technology (BMK) and for Labour and Economy (BMAW), represented by the Austrian research funding association (FFG), and the federal states of Styria, Upper Austria and Tyrol.

8. References

1. DIN 54183:2018-02, Non-Destructive Testing - Thermographic Testing - Eddy-Current Excited Thermography Available online: <https://www.din.de> (accessed on 31 January 2018).
2. Netzelmann, U.; Walle, G.; Lugin, S.; Ehlen, A.; Bessert, S.; Valeske, B. Induction Thermography: Principle, Applications and First Steps towards Standardisation. *Quantitative InfraRed Thermography Journal* **2016**, *13*, 170–181, doi:10.1080/17686733.2016.1145842.
3. Srajbr, C. Induction Excited Thermography in Industrial Applications. In Proceedings of the 19th World Conference on Non-Destructive Testing; Munich, Germany, June 2016; pp. 13–17.
4. Oswald-Tranta, B. Induction Thermography for Surface Crack Detection and Depth Determination. *Applied Sciences* **2018**, *8*, 257, doi:10.3390/app8020257.
5. U.Ossberger; S. Eck; E. Stocker Performance of Different Materials in a Frog of a Turnout. **2015**, doi:10.13140/RG.2.1.2549.7442.
6. Xu, W.; Li, X.; Zhang, J.; Xue, Z.; Cao, J. Ultrasonic Signal Enhancement for Coarse Grain Materials by Machine Learning Analysis. *Ultrasonics* **2021**, *117*, 106550, doi:10.1016/j.ultras.2021.106550.
7. Tuschl, C.; Oswald-Tranta, B.; Eck, S.; Dornig, P. Scanning Pulse Phase Thermography for Surface Defect Detection in Manganese Steel Turnout Frogs. *ReJNDT* **2023**, *1*, doi:10.58286/28220.
8. Netzelmann, U.; Walle, G.; Ehlen, A.; Lugin, S.; Finckbohner, M.; Bessert, S. NDT of Railway Components Using Induction Thermography. *AIP Conference Proceedings* **2016**, *1706*, 150001, doi:10.1063/1.4940613.
9. Vaibhav, T.; Balasubramaniam, K.; Kidangan, R.; Bose, A. Eddy Current Thermography for Rail Inspection. In Proceedings of the 13th QIRT Conference; Gdansk, Poland, January 1 2016.
10. D'Accardi, E.; Dell'Avvocato, G.; Masciopinto, G.; Marinelli, G.; Fumarola, G.; Palumbo, D.; Galietti, U. Evaluation of Typical Rail Defects by Induction Thermography: Experimental Results and Procedure for Data Analysis during High-Speed Laboratory Testing. *Quantitative InfraRed Thermography Journal* **2024**, *1–22*, doi:10.1080/17686733.2024.2340060.
11. Tuschl, C.; Oswald-Tranta, B.; Eck, S. Inductive Thermography as Non-Destructive Testing for Railway Rails. *Applied Sciences* **2021**, *11*, 1003, doi:10.3390/app11031003.
12. Stock, R.; Pippan, R. RCF and Wear in Theory and Practice—The Influence of Rail Grade on Wear and RCF. *Wear* **2011**, *271*, 125–133, doi:10.1016/j.wear.2010.10.015.
13. IRCAM Velox 1310k SM Datasheet Available online: https://www.ircam.de/wp-content/uploads/2021/02/IRCAM_VELOX1310kSM_10%C2%B5m_Datasheet.pdf (accessed on 9 June 2022).